Dielectric response of the water hydration layer around spherical solutes

Christian Schaaf* and Stephan Gekle†

Biofluid Simulation and Modeling, Department of Physics, University of Bayreuth, 95440 Bayreuth, Germany

(Received 1 December 2014; revised manuscript received 31 August 2015; published 18 September 2015)

We calculate the local dielectric function $\varepsilon(r)$ inside the hydration layer around a spherical solute (i) from molecular dynamics simulations including explicit solutes and (ii) theoretically using the nonlocal dielectric function of bulk water which includes the radial electric field, but not the explicit solute. The observed agreement between the two concepts shows that while $\varepsilon(r)$ is strongly different from bulk, this difference is not due to restructuring of the hydrogen bond network but is mostly a consequence of the field geometry. The dielectric response differs for anions and cations, yielding a natural explanation for the well-known charge asymmetry of ionic solvation in agreement with experimental data.

DOI: 10.1103/PhysRevE.92.032718 PACS number(s): 87.15.kr, 61.20.Gy, 61.20.Ja, 77.22.−d

The dielectric constant of liquid solvents such as water determines the local screening of an electric field due to solvent molecules. It is therefore a key parameter to describe the interaction between partially charged protein moieties [1–6], the solvation and distribution of salt ions [7–12], ion-specific (Hofmeister) effects [13,14], electrokinetic processes [15,16], and even quantum effects such as incoherent energy transfer in organic semiconductors [17]. As a consequence, it features prominently in the Bjerrum length, in the Debye length, as well as in the Förster radius, which represent the length scales commonly used to describe the above processes [18]. The dielectric constant furthermore is an essential ingredient in modern simulation techniques such as implicit solvent molecular dynamics [19–21], Monte Carlo schemes [22,23], and quantum simulations [24].

This importance in very different fields explains the recent upsurge in attempts to obtain quantitative data for the spatially resolved local dielectric constant $\varepsilon(r)$ on the nanometer scale either from dielectric spectroscopy experiments [25–34] or from computer simulations [35–47]. It is generally found that the dielectric properties in the close vicinity of interfaces are fundamentally different than in bulk.

In some contrast to these local attempts stand a number of approaches to calculate solvation energies and particle-particle interaction forces from pure bulk water quantities based on the concept of a wave-vector-dependent, nonlocal dielectric constant $\varepsilon(k)$ [48–55]. This quantity has been obtained from molecular dynamics (MD) simulations in excellent agreement with experiments [56,57]. Its first applications, however, date back much earlier and were based on *ad hoc* assumptions on the shape of $\varepsilon(k)$ [58].

Here we unify both approaches by demonstrating that the radial component of the spatially resolved local $\varepsilon(r)$ surrounding spherical solutes such as ions or small protein side groups in water, as calculated from explicit MD simulations using a newly developed formalism, is in good agreement with that obtained from the nonlocal dielectric constant $\varepsilon(k)$ in bulk water. Our work demonstrates that, while the local dielectric response in the hydration layer of the central charged object is severely different from bulk, this difference is not mainly due to a restructuring of the local hydrogen bond network but instead is a manifestation of molecular correlations existing already in bulk water. The obtained dielectric profiles furthermore furnish an explicit explanation for the well-known asymmetry in the solvation energy of equally sized cations and anions and compare favorably with experimental data.

I. METHODS

A. Simulations

We conduct classical MD simulations of 6017 extended simple point charge (SPC/E) water molecules arranged in a spherical droplet of radius $R_{\mathrm{drop}} = 3.8\,\mathrm{nm}$ enclosed by wall particles with Lennard-Jones interaction parameters $\sigma_{eO} = 0.25\,\mathrm{nm}$ and $\epsilon_{eO} = 0.62\,\mathrm{kJ/mol}$ (see Fig. 1). Since the SPC/E force field is nonpolarizable, effects due to electronic polarization are not explicitly accounted for in our simulations. The solute is fixed in the center of the sphere, leading to a completely radially symmetric system. Note that in the more common setup of an ion in a cubic simulation box the radial symmetry is broken, rendering the derivation of a linear response theory unnecessarily complicated. We have checked that our results are independent of the droplet size (see Fig. S1 of the Supplemental Material (SM) [59]), thus faithfully reproducing the situation of an ion solvated in bulk water. Simulations are run using GROMACS [60] together with the force fields of [61] for the ions (see Table I). For visualization we use the VMD package [62].

Table II lists the simulation times for the calculations with the different solutes. For the van der Waals potential we use a cutoff radius of 1 nm (switched after 0.9 nm). The droplet is centered in a cubic cell with an edge length of 12 nm, i.e., much larger than the drop radius. We simulate our systems as NVT ensemble with a sampling rate of 0.2 ps. To keep the temperature at 300 K we use a Nosé-Hoover thermostat.

For the electrostatics, we use the particle mesh Ewald summation (PME) [63] with the real-space Coulomb interactions truncated after 1.5 nm and switched at 1.45 nm. In each direction 80 k-vectors are used. We note that by symmetry the radial dipole moment vanishes identically at every instant when integrating over the entire simulation box. We thus expect no effects due to interaction between the different periodic images when using Ewald summation. To verify

*christian.schaaf@uni-bayreuth.de
†stephan.gekle@uni-bayreuth.de

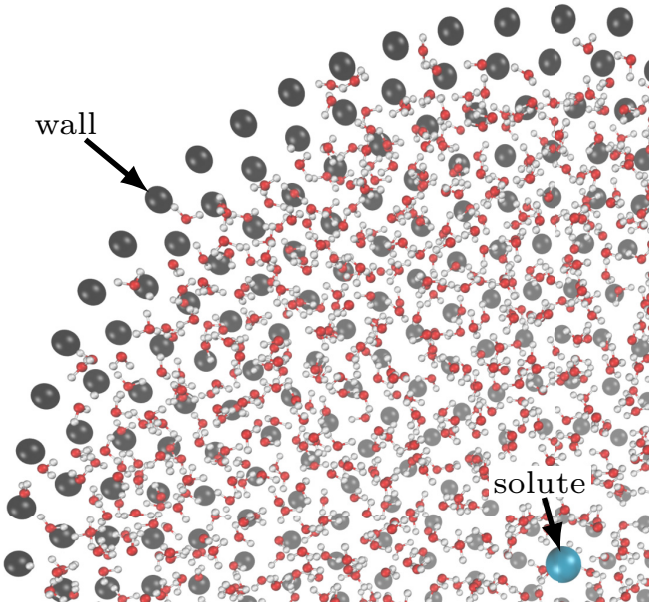

FIG. 1. (Color online) Cut through the simulated system: the sphere in the center of the droplet is the solute; the black spheres are the wall particles.

this expectation explicitly we conduct a simulation without periodic images where electrostatic (and Lennard-Jones) interactions are calculated with a cutoff larger than the drop diameter. All the interactions within our finite-sized system are thus fully and explicitly included in the simulation without any periodic images. Figure S2 (in the SM) demonstrates that this approach leads to the same results, thus validating our use of Ewald summation in the main text. The high computational cost of this approach, however, precludes its use for large-scale production runs.

The nonlocal response function was extracted from bulk water simulations in a cubic box with an edge length of 10 nm containing 33 226 water molecules and a simulation time of 32 ns. The cutoff for the Coulomb interactions was 1.1 nm with a switch radius of 0.9 nm. The other parameters were the same as for the simulation with explicit ions.

B. Linear response

For a general system the local dielectric permittivity $\boldsymbol{\varepsilon}(\boldsymbol{r})$ is a tensor of rank 2. Due to the spherical symmetry of our system this tensor becomes diagonal with two components for radial and tangential fields. Here we concentrate on the radial component $\varepsilon_r(r)$ depending on the distance r from the solute.

TABLE I. Ion-water oxygen force field parameters from Ref. [61] as used in this work.

Ion	σ_{iO} (nm)	ϵ_{iO} (kJ/mol)
Na^+	0.2876	0.5216
Cs^+	0.333	0.5
Cl^-	0.3785	0.5216
I^-	0.425	0.32

TABLE II. Simulation time of the different systems.

Particle type	Time (ns)
Model solute ($\sigma_{iO} = 0.4$ nm, $\epsilon_{iO} = 0.65$ kJ/mol)	820
Model solute ($\sigma_{iO} = 0.31$ nm, $\epsilon_{iO} = 0.65$ kJmol)	145
Model solute ($\sigma_{iO} = 0.4$ nm, $\epsilon_{iO} = 1.54$ kJ/mol)	145
Repulsive potential	145
Uncharged ions (Na, Cs, Cl, I)	220
Charged ions (Na^+, Cs^+, Cl^-, I^-)	80

Applying the linear response formalism we obtain [for details see Eq. (A10) of the Appendix]

$$\varepsilon_r^{-1}(r) = 1 - \frac{4\pi\beta r^2}{\varepsilon_0}(\langle P_r(r)M_r\rangle_0 - \langle P_r(r)\rangle_0\langle M_r\rangle_0), \quad (1)$$

where $\langle\cdot\rangle_0$ denotes the ensemble average for the unperturbed system, $P_r(r)$ is the radial polarization, R_{drop} is the radius of our droplet, $\beta = (k_B T)^{-1}$ is the inverse thermal energy, ε_0 is the vacuum permittivity, and M_r is given by $M_r = \int_0^{R_{\text{drop}}} P_r(r')dr'$.

To calculate $P_r(r)$ we go beyond the dipole approximation which is often insufficient near interfaces [42,64]. Instead, we use the internal charge density $\rho^{\text{int}}(r)$, thus taking all electric moments into account as derived in Eq. (A18) of the Appendix.

C. Nonlocal dielectric constant

In the nonlocal treatment, the polarization of the dielectric medium at position $\boldsymbol{r}$ depends on the electric field at any other point $\boldsymbol{r}'$, which leads to an integral equation

$$\boldsymbol{P}(\boldsymbol{r}) = \varepsilon_0 \int_V (\varepsilon_{nl}(\boldsymbol{r},\boldsymbol{r}') - 1)\boldsymbol{E}^{\text{int}}(\boldsymbol{r}')d\boldsymbol{r}'. \quad (2)$$

In an isotropic, homogeneous bulk system the response function $\varepsilon_{nl}(\boldsymbol{r},\boldsymbol{r}')$ in Eq. (2) depends only on the distance $|\boldsymbol{r} - \boldsymbol{r}'|$ leading to a local expression in Fourier space as a function of the wave vector k:

$$\boldsymbol{P}(k) = \varepsilon_0(\varepsilon_{nl}(k) - 1)\boldsymbol{E}(k). \quad (3)$$

The quantity $\varepsilon_{nl}(k)$ can be calculated from MD simulations of a bulk water box without solutes using the structure factor [56]

$$\varepsilon_{nl}(k) = \left[1 - \frac{1}{\varepsilon_0 k_B T}\frac{\langle\rho(k)\rho(k)\rangle}{k^2}\right]^{-1}, \quad (4)$$

where $\rho(k)$ is the Fourier transform of the water charge distribution. To use the advantage of the fast Fourier transform (FFT) these charges were distributed on a grid similar to the PME method [65].

II. RESULTS AND DISCUSSION

We first consider the water density profile as function of the distance r from the solute as shown in Fig. 2(a) for three solute particles. The first is a Lennard-Jones sphere similar to water's oxygen ($\epsilon_{iO} = 0.65$ kJ/mol), the second is a very hydrophilic particle (1.54 kJ/mol), and the third possesses a purely repulsive potential of the form $V(r) = (\sigma_{iO}/r)^{12}$. For all three solutes, $\sigma_{iO} = 0.40$ nm, corresponding to iodide. We find an oscillatory density profile with a wavelength of $\lambda \approx 0.28$ nm.

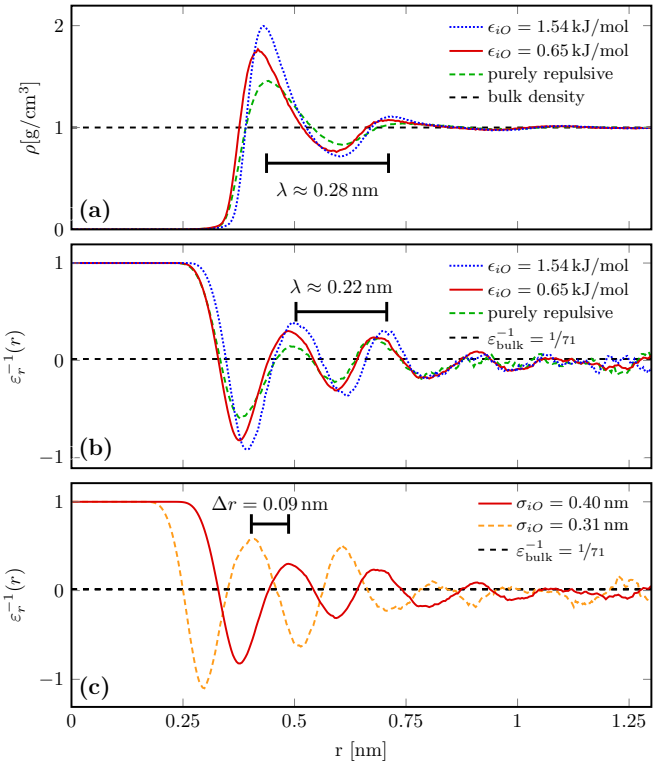

FIG. 2. (Color online) (a) The radial density profiles around three different solutes ranging from purely repulsive (hydrophobic) to very attractive (hydrophilic). (b) The inverse radial component of the local dielectric permittivity shows strongly oscillatory behavior but with a shorter wavelength than the density oscillations. Interestingly, the oscillating permittivity is almost independent of the water-ion interaction parameters. (c) Changing the Lennard-Jones interaction distance (ion size) σ_{iO} leads to a shift but not to qualitative changes in the dielectric profiles.

Using Eq. (1) we now calculate the radial component of the spatially dependent dielectric tensor $\varepsilon_r(r)$ as shown in Fig. 2(b) for the same three particles. This distance-dependent $\varepsilon_r(r)$ will be relevant whenever two solutes come into close contact, e.g., side groups of the same protein, while bulk measurements on salt solutions will report a spatial average. Oscillatory behavior is found which for distances $r > 1.1$ nm decreases to the bulk value $\varepsilon_{\mathrm{bulk}}^{-1} = \frac{1}{71}$ of SPC/E water [66]. Yet, close to the solute the oscillations in $\varepsilon_r(r)$ possess a shorter wavelength and decay much slower than the density oscillations. Our most important finding in Fig. 2(b) is that the profile of the dielectric constant is virtually independent of the depth of the potential, meaning that any difference in the dielectric response is caused by the size of the ion and not by specific ion-water interactions. Dispersion interactions between ion and water thus do not play a crucial role for the dielectric profiles.

We proceed to investigate the dependence of $\varepsilon_r(r)$ on the solute size by varying the Lennard-Jones interaction distance σ_{iO} between 0.31 nm (corresponding roughly to Na^+) and 0.40 nm (corresponding roughly to I^-). The dielectric profiles shown in Fig. 2(c) are shifted by the same difference of 0.09 nm, yet the amplitudes of the oscillations are hardly influenced.

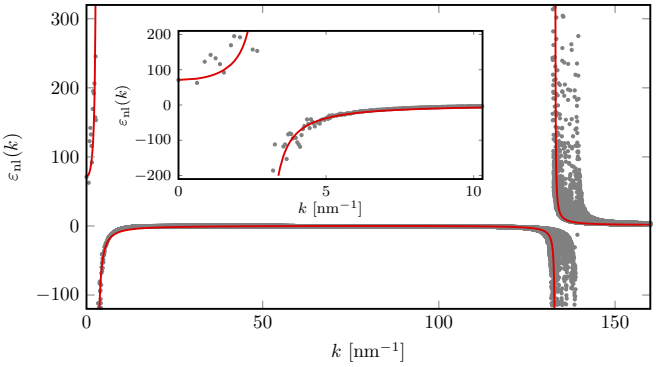

FIG. 3. (Color online) The nonlocal dielectric response of bulk water calculated from our MD simulations (gray dots) and the corresponding empirical fit function (solid line). Due to the singularity for $k = 0$ we add the bulk value [66] for SPC/E, $\varepsilon_{nl}(k = 0) = 71$, manually [56].

A. Relation to nonlocal bulk dielectric

Motivated by our observation that the dielectric profile is almost uninfluenced by the properties of the solute particle (interaction potential and size), we suspect that the drastic changes in the radial interfacial dielectric constant, as observed in Figs. 2(b) and 2(c), may be related to the complex structure of (bulk) water itself rather than to any specific restructuring effects in the ionic solvation shell. In the following, we therefore attempt to calculate the dielectric profiles from the properties of pure bulk water.

Our starting point is the nonlocal wave-vector-dependent dielectric function $\varepsilon_{nl}(k)$ which we obtain from a simulation of bulk water. As shown in Fig. 3 we observe two poles at $k_1 \approx 2.9\,\mathrm{nm}^{-1}$ and $k_2 \approx 133\,\mathrm{nm}^{-1}$ in good agreement with earlier MD calculations [56] for a different water model.

In order to relate the nonlocal bulk quantity $\varepsilon_{nl}(k)$ to the local dielectric constant $\varepsilon_r(r)$ around the solute, we follow a model developed by Basilevsky and Parsons [49,51]. Here, the ion is considered a spherical cavity filled with vacuum and a point charge at its center. The cavity is surrounded by bulk water being a nonlocal dielectric medium described by $\varepsilon_{nl}(k)$. The electrostatic potential $\Psi(r)$ inside the solvent is then given by three contributions [51]: the external potential of the solute, the contribution of the surface charge, and the potential due to the induced charge distribution in the dielectric medium. Thus,

$$\Psi(r) = \frac{Q}{4\pi\varepsilon_0 r} + \frac{a^2\sigma}{\varepsilon_0 r} + \xi(r), \tag{5}$$

where Q is the ion charge and the ion radius a is obtained from Fig. 2(c) as the radial position where the $\varepsilon_r^{-1}(r)$ curves first deviate from 1. The contribution of the induced charge distribution can be calculated using

$$\xi(r) = \frac{1}{2\varepsilon_0}\int_a^\infty dr' g(r')(r + r' - |r - r'|)\frac{r'}{r}, \tag{6}$$

where $g(r)$ is given by the solution of the following Fredholm integral equation as detailed in [51]:

$$g(r) + \int_a^\infty dr' \gamma(r,r') g(r') = -\left(\frac{Q}{4\pi a^2} + \sigma\right)\gamma(r,a). \tag{7}$$

The auxiliary function $\gamma(r,r')$ involves only known quantities and is given as [51]

$$\gamma(r,r') = \gamma_L(r,r') + \gamma_{p1}(r,r') + \gamma_{p2}(r,r') \tag{8}$$

with

$$\gamma_L(r,r') = -\frac{\chi_L}{2\lambda}\frac{r}{r'}\{\exp[-(r+r')/\lambda] - \exp(-|r-r'|/\lambda)\}$$

$$\gamma_{pi}(r,r') = -\frac{\chi_{pi}k_i}{2}\frac{r}{r'}\{\sin[k_i(r+r')] - \sin(k_i|r-r'|)\}.$$

The parameters χ_L, χ_{pi}, and λ can be obtained directly from the nonlocal bulk permittivity, which we calculate using Eq. (4). The result is shown in Fig. 3 as gray points. As the subsequent calculations require the inverse Fourier transform of $\varepsilon_{nl}(k)$ to real space and the evaluation of spatial integrals, we follow [51] and describe the form of $\varepsilon_{nl}(k)$ as

$$\varepsilon_{nl}(k) = 1 + \frac{\chi_L}{1+\lambda^2k^2} + \frac{\chi_{p1}}{1-(k/k_1)^2} - \frac{\chi_{p2}}{1-(k/k_2)^2}. \tag{9}$$

With this form, the integrals in the subsequent equations can be performed analytically, thus avoiding the numerically unstable integration over the poles in $\varepsilon_{nl}(k)$. The required parameters are obtained by first fixing the positions of the two poles k_1 and k_2 and the sum of the amplitudes

$$1 + \chi_l + \chi_{p1} - \chi_{p2} = \epsilon(k=0) = 71. \tag{10}$$

The wavelength λ and the amplitudes are chosen as

$$\begin{aligned} k_1 &= 2.9\,\mathrm{nm}^{-1}, \quad k_2 = 133\,\mathrm{nm}^{-1}, \\ \lambda &= 0.025, \quad \chi_L = -1{,}696, \\ \chi_{p1} &= 72.13, \quad \chi_{p2} = 0{,}377, \end{aligned} \tag{11}$$

in order to obtain a satisfying agreement with our MD results as shown by the red solid line in Fig. 3. These parameters satisfy the stability criteria for the nonlocal permittivity [57] $\varepsilon_{nl}(k) > 1$ or $\varepsilon_{nl}(k) < 0$. We emphasize that we use Eq. (9) as a purely empirical form in order to obtain a numerically stable form of the integral equation, Eq. (7). A physical interpretation of Eq. (9) in terms of molecular geometry is beyond the scope of the present paper.

We furthermore apply the regularization procedure for the integral equation using the regularization parameter $\alpha = 0.2$ [51].

Finally, the surface charge σ is used here as an adjustable parameter which is chosen as $\sigma = 0.65\ e/\mathrm{nm}^2$ for $\sigma_{iO} = 0.31$ nm and $\sigma = 0.2\ e/\mathrm{nm}^2$ for $\sigma_{iO} = 0.4$ nm. Both values lie in between the limiting values for a simple local model of bulk water $\sigma_b = -\frac{Q}{a^2}(1-\frac{1}{71}) = 6\ e/\mathrm{nm}^2$ and for vacuum $\sigma_{\mathrm{vac}} = 0$. For not too large values of the surface charge $\sigma \leqslant 2\ e/\mathrm{nm}^2$ the effect on the resulting dielectric profile is negligible (see Fig. S4 of the SM).

We are now in a position to compute the local inverse permittivity purely from bulk quantities. For this we use the ratio of the internal to the external electric field:

$$\varepsilon_r^{-1}(r) = \frac{E^{\mathrm{int}}(r)}{E^{\mathrm{ext}}(r)} = \frac{-\nabla\Psi(r)}{Q/(4\pi\varepsilon_0 r^2)}. \tag{12}$$

As demonstrated by Fig. 4, the results agree very well with those obtained above from the system including the solute explicitly. This demonstrates that the radial dielectric constant

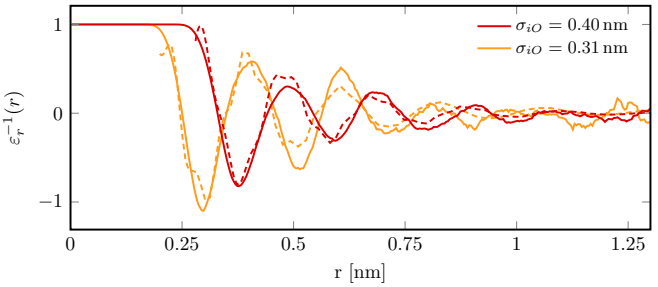

FIG. 4. (Color online) Comparison of the local dielectric constant calculated from MD simulation including explicit ions from Fig. 2(c) (solid lines) to the same quantity obtained solely from bulk water properties using the nonlocal model of [51] with $\varepsilon_{nl}(k)$ from our bulk MD simulations (dashed lines). The good agreement demonstrates that the response around a spherical solute is mostly determined by bulk water properties and not so much caused by a restructuring of water in the hydration layer.

of the solvation shell around simple ions can indeed be determined to a large extent from water bulk properties and the radial field geometry showing that the water structure in the hydration layer is not significantly perturbed [67]. We speculate that recent dielectric spectroscopy experiments [31,32,34,68–70] might, at least in part, be explainable based on water's complex bulk properties in a similar manner if the approach described in the present paper is extended to the frequency-dependent dielectric function.

B. Charged solutes

We now consider the change in the dielectric profiles when the spherical solute bears an electrical charge, as is the case for salt ions or charged protein side groups. As shown in Fig. 5(a), we find that the permittivity for negative charges (dashed lines) is shifted to smaller radii although the Lennard-Jones diameter σ_{iO} is held constant. For positive charges (solid lines), on the other hand, mainly the amplitude of the dielectric profiles changes but no significant shift is observed. This asymmetry is related to the asymmetric character of the water molecule. While the small partially positively charged hydrogen atom can be attracted easily by a negatively charged solute, a similarly close attraction of the oxygen atom by a positively charged solute is hindered by the comparatively large size of the oxygen. Indeed, for $q = \pm 1$ the shift between the first mimima is around 0.1 nm which corresponds to the length of the intramolecular OH bond in water.

This different behavior of hydrogen and oxygen in the solvation shell around anions and cations was recognized a long time ago as an explanation for the asymmetry in solvation energy of (equally sized) anions and cations [72]. This phenomenon cannot be reproduced by the classical Born theory which is charge-sign symmetric [73], which led to the introduction of effective charge-dependent ion radii into continuum theories [74–78]. The shift in the dielectric profiles around differently charged particles observed in Fig. 5 points in the same direction.

In order to obtain a more quantitative explanation, we proceed to calculate the solvation energy based on our dielectric profiles. Our central assumption is that the solvation

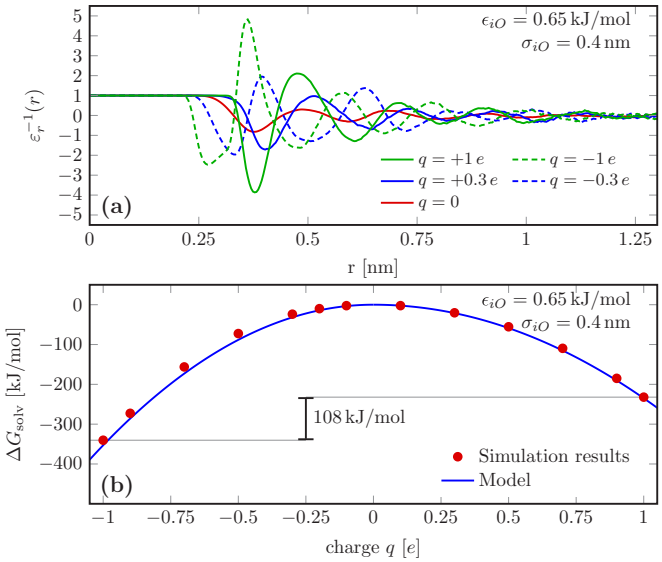

FIG. 5. (Color online) (a) Radial dielectric profile around a charged solute. The dielectric profiles around the positive charges show almost no phase shift but a slightly larger amplitude compared to $q = 0$. The profiles around the negative charges are shifted towards a smaller radius. (b) The solvation energy for different partially charged solutes (dots) calculated solely from dielectric profiles as those shown in (a). The results show an asymmetry of the solvation energy of 108 kJ/mol in good agreement with full free-energy calculations [71].

energy is determined mainly by the change in electrostatic energy as the dielectric solvent experiences the electric field caused by the ion, i.e., neglecting contributions from a static potential due to water orientation [71], or entropic effects such as the creation of a cavity. In order to account for possible nonlinear effects, we divide the process of charging into a series of steps increasing the charge by small amounts in each step. The change in the solvation energy $\Delta G_{\text{solv}}^{i\to i+1}$ between steps i and $i+1$ is then calculated using the dielectric profile $\varepsilon_{r,i}$ around the solute with charge q_i [see Eq. (A21) in the Appendix]:

$$\Delta G_{\text{solv}}^{i\to i+1} = \underbrace{\frac{1}{8\pi\varepsilon_0}\int_0^{R_{\text{drop}}} (\varepsilon_{r,i}^{-1}(r) - 1)\frac{1}{r^2}dr}_{:=L} \left(q_{i+1}^2 - q_i^2\right). \tag{13}$$

We checked that the drop radius R_{drop} is sufficiently large and does not influence the results (see Table S1 of the SM). The thus calculated solvation energy for different charges of our model ion with $\sigma_{iO} = 0.4$ nm is shown by the dots in Fig. 5(b). The resulting charge asymmetry between $q = \pm 1e$ is 108 kJ/mol. This value, which is derived without any adjustable parameters solely from dielectric profiles such as those in Fig. 5(a), compares favorably with the charge asymmetry of 83.7 kJ/mol determined from full free-energy calculations for an ion composed of individual Lennard-Jones spheres with a total radius 0.4 nm, which is similar (but not identical) to our system [71].

As demonstrated by the solid line in Fig. 5(b) our data are well described by a quadratic form $\Delta G_{\text{solv}} = L^{\pm}q^2$. The coefficient L^+ for positive ions is directly calculated from the dielectric profile around $q = 0$ as shown in Eq. (13) while L^- is obtained by shifting the same profile 0.09 nm towards a smaller radius corresponding to the shift between the two first minima of $q = \pm 1\,e$ in Fig. 5(a). We obtain $L^{(+)} = -234.9$ kJ/mol/e^2 and $L^{(-)} = -353.0$ kJ/mol/e^2 which is similar to the results for the chloride-sized ion in [71] (see [79]). Therefore, nonlinear dielectric effects appear to affect the solvation free energy only through the sign, but not the magnitude, of the ion charge. This observation, which was noted earlier by Bardhan *et al.* [71], may be understood to some extent by inspection of Fig. 5(b), where the height of the positive and negative peaks of $\varepsilon_r(r)$ is scaled up roughly in an equal manner as the charge q is increased leading to canceling contributions in Eq. (13).

TABLE III. The calculated solvation energies $\Delta G_{\text{solv}}^{\text{calc}}$ agree fairly well with the experimental values $\Delta G_{\text{solv}}^{\text{exp}}$. The deviations can be attributed to entropic effects that are not accounted for in the present framework.

		$\Delta G_{\text{solv}}^{\text{exp}}$ (kJ/mol)	
Ion	$\Delta G_{\text{solv}}^{\text{calc}}$ (kJ/mol)	Ref. [81]	Ref. [80]
Na^+	−429	−424	−371
Cs^+	−328	−306	−253
Cl^-	−388	−304	−373
I^-	−328	−243	−311

In order to verify further the validity of our calculations we use the framework established above to calculate the solvation free energies of Na^+, Cs^+, Cl^-, and I^- ions. The corresponding dielectric profiles are shown in Fig. S3 of the SM. Table III shows that our results are in fair agreement with available experimental data which themselves scatter over a fairly large range of 50 to 70 kJ/mol which is due to the large uncertainty of free solvation energy of a proton. Our calculated values are slightly more negative than the experimental values for both anions and cations, which is not surprising as we neglect entropic effects due to the creation of the cavity. These are negative for all ions considered [80,81], contribute with a negative sign to the free energy, and would thus bring our values closer towards the experimental data.

III. CONCLUSION

We extracted the radial component of the dielectric response of water around a spherical solute from classical molecular dynamics simulations using two fundamentally different approaches: the first is based on the concept of a spatially dependent, yet local, dielectric constant $\varepsilon_r(r)$ while the second approach departs from the nonlocal wave-vector-dependent dielectric function $\varepsilon(k)$ of bulk water. We find that both concepts exhibit good agreement, showing a strongly oscillatory behavior of $\varepsilon_r(r)$ as a function of the distance to the solute. The agreement demonstrates that even the drastic change in the radial component of the static local dielectric constant around a spherical solute can be explained by water's nonlocal bulk properties without the need to invoke a change in water structure. For charged solutes we find a pronounced asymmetry between cations and anions: while the former

modify mainly the amplitude of the oscillations in $\varepsilon_r(r)$ compared to an uncharged solute, the dielectric profiles of the latter are significantly shifted towards smaller radii. This shift provides a direct explanation for the commonly held view that anions appear to be "dielectrically smaller" than their positively charged counterparts.

Our detailed dielectric profiles can furthermore be useful for the calculation of attractive and repulsive forces between charged side groups in proteins, for the improvement of implicit solvent simulation models or for understanding cosolvent effects in protein folding. Extending our methodology to the frequency-dependent dielectric function may shed new light onto recent experiments [31,32,34,68] where changes in the dielectric spectrum are often related to changes in the local water structure and dynamics around the solvated molecule. Based on our results we speculate that only part of the observed spectral changes may be caused by a restructuring of interfacial water while the other part may be traced back directly to the complex structure of bulk water itself.

ACKNOWLEDGMENTS

The authors gratefully acknowledge funding from the Volkswagen Foundation and the Deutsche Forschungsgemeinschaft Graduiertenkolleg 1640. Computing time has been granted by the John von Neumann Institute for Computing (NIC) and provided on the supercomputer JUROPA at Jülich Supercomputing Centre (JSC).

APPENDIX: DETAILED DERIVATIONS

1. Radial component of the inverse dielectric permittivity

The electric field due to a point charge in vacuum is

$$\boldsymbol{E}^{\mathrm{ext}}(r) = \frac{1}{4\pi\varepsilon_0}\frac{q}{r^2}\hat{e}_r. \tag{A1}$$

Assuming an infinitely large dielectric with spherical symmetry and the point charge located in the center the internal electric field is

$$\boldsymbol{E}^{\mathrm{int}}(r) = \frac{1}{4\pi\varepsilon_0\varepsilon_r(r)}\frac{q}{r^2}\hat{e}_r, \tag{A2}$$

leading to a relation between the radial components of both fields:

$$E_r^{\mathrm{int}}(r) = \frac{E_r^{\mathrm{ext}}}{\varepsilon_r(r)}. \tag{A3}$$

The internal electric field creates a radial polarization $\Delta P_r(r)$ of the medium:

$$\Delta P_r(r) = \varepsilon_0(\varepsilon_r(r)-1)E_r^{\mathrm{int}}(r) = \frac{\varepsilon_r(r)-1}{\varepsilon_r(r)}\frac{q}{4\pi r^2}. \tag{A4}$$

We next calculate the same quantity (mean polarization) by using statistical mechanics. The mean value for the NVT system with applied external electric field is

$$\langle \boldsymbol{P}\rangle_q = \frac{\int \boldsymbol{P}e^{-\beta(\mathcal{H}+W(q))}d\boldsymbol{\Gamma}}{\int e^{-\beta(\mathcal{H}+W(q))}d\boldsymbol{\Gamma}}, \tag{A5}$$

where $\mathcal{H}$ is the Hamiltonian of the unperturbed system and $W(q)$ is the energy shift due to the external field:

$$\begin{aligned} W(q) &= -\int \boldsymbol{E}^{\mathrm{ext}}\cdot\boldsymbol{P}d\boldsymbol{r} \\ &= -4\pi\int_0^{R_{\mathrm{drop}}} E_r^{\mathrm{ext}}(r)P_r(r)r^2dr \\ &= -\frac{q}{\varepsilon_0}\int_0^{R_{\mathrm{drop}}} P_r(r)dr. \end{aligned} \tag{A6}$$

For small perturbations q one can linearize Eq. (A5):

$$\begin{aligned} \langle \boldsymbol{P}\rangle_q &\approx \langle \boldsymbol{P}\rangle_0 + q\frac{\partial\langle \boldsymbol{P}\rangle}{\partial q} \\ &= \langle \boldsymbol{P}\rangle_0 - \beta q\left\{\left\langle \boldsymbol{P}\frac{\partial W}{\partial q}\right\rangle_0 - \langle \boldsymbol{P}\rangle_0\left\langle\frac{\partial W}{\partial q}\right\rangle_0\right\}, \end{aligned} \tag{A7}$$

where $\langle\cdot\rangle_0$ denotes averaging of the system without an external field. As we are interested in the change of the polarization, $\Delta\boldsymbol{P}$, we can write

$$\Delta\boldsymbol{P} = -\beta q\left\{\left\langle \boldsymbol{P}\frac{\partial W}{\partial q}\right\rangle_0 - \langle \boldsymbol{P}\rangle_0\left\langle\frac{\partial W}{\partial q}\right\rangle_0\right\}. \tag{A8}$$

Combining Eqs. (A4), (A6), and (A8) gives

$$\frac{\varepsilon_r(r)-1}{\varepsilon_r(r)} = \frac{4\pi\beta r^2}{\varepsilon_0}(\langle P_r(r)M_r\rangle_0 - \langle P_r(r)\rangle_0\langle M_r\rangle_0) \tag{A9}$$

with

$$M_r = \int_0^{R_{\mathrm{drop}}} P_r(r')dr'.$$

This leads to the final expression given as Eq. (1) in the main text:

$$\varepsilon_r^{-1}(r) = 1 - \frac{4\pi\beta r^2}{\varepsilon_0}(\langle P_r(r)M_r\rangle_0 - \langle P_r(r)\rangle_0\langle M_r\rangle_0). \tag{A10}$$

2. Polarization from charge distribution

As the radial field is perpendicular to all dielectric boundaries in the system, the displacement field is continuous including the boundary of the droplet:

$$\varepsilon_0 E_r^{\mathrm{ext}} = \varepsilon_0 E_r^{\mathrm{int}} + P_r. \tag{A11}$$

The internal electric field is the sum of the external field and the electric field due to the polarization:

$$\varepsilon_0 E_r^{\mathrm{ext}}(r) = \varepsilon_0 E_r^{\mathrm{ext}}(r) + \varepsilon_0 E_r^{\mathrm{pol}}(r) + P_r(r), \tag{A12}$$

so we get

$$P_r(r) = -\varepsilon_0 E_r^{\mathrm{pol}}(r). \tag{A13}$$

Using the Gauss theorem we get

$$\nabla\cdot\boldsymbol{E}^{\mathrm{pol}}(r) = \frac{\rho^{\mathrm{int}}(r)}{\varepsilon_0}, \tag{A14}$$

where the internal charge density $\rho^{\mathrm{int}}(r)$ consists of the partial charges of the molecules. Using again the spherical symmetry

we get

$$\frac{1}{r^2}\frac{\partial}{\partial r}\left(r^2 E_r^{\mathrm{pol}}(r)\right) = \frac{\rho^{\mathrm{int}}(r)}{\varepsilon_0}, \tag{A15}$$

$$\left[r^2 E_r^{\mathrm{pol}}(r')\right]_0^r = \int_0^r \frac{r'^2 \rho^{\mathrm{int}}(r')}{\varepsilon_0} dr', \tag{A16}$$

$$r^2 E_r^{\mathrm{pol}}(r) - 0 = \int_0^r \frac{r'^2 \rho^{\mathrm{int}}(r')}{\varepsilon_0} dr'. \tag{A17}$$

Combining Eqs. (A13) and (A17), one gets

$$P_r(r) = -\frac{1}{r^2}\int_0^r r'^2 \rho^{\mathrm{int}}(r') dr'. \tag{A18}$$

3. Derivation of the solvation energy

The change in the field energy due to the dielectric medium is given by

$$\Delta W_{\mathrm{el}} = \frac{1}{2}\int_V \left(\boldsymbol{D}\cdot\boldsymbol{E}^{\mathrm{int}} - \boldsymbol{D}_0\cdot\boldsymbol{E}^{\mathrm{ext}}\right) dV, \tag{A19}$$

where $\boldsymbol{D}$ is the displacement field inside the medium and $\boldsymbol{D}_0$ the displacement field in vacuum. (Note that for the present geometry $\boldsymbol{D} = \boldsymbol{D}_0$.) Using the relations $\boldsymbol{D} = \varepsilon_0\varepsilon\boldsymbol{E}^{\mathrm{int}}$ and $\boldsymbol{D}_0 = \varepsilon_0\boldsymbol{E}^{\mathrm{ext}}$ yields

$$\Delta W_{\mathrm{el}} = \frac{1}{2}\varepsilon_0\int_V \left(\varepsilon\boldsymbol{E}^{\mathrm{int}}\cdot\boldsymbol{E}^{\mathrm{int}} - \boldsymbol{E}^{\mathrm{ext}}\cdot\boldsymbol{E}^{\mathrm{ext}}\right) dV. \tag{A20}$$

We now use that $\boldsymbol{E}^{\mathrm{int}} = \varepsilon^{-1}\boldsymbol{E}^{\mathrm{ext}}$ and $\boldsymbol{E}^{\mathrm{ext}} = \frac{1}{4\pi\varepsilon_0}\frac{q}{r^2}\frac{\boldsymbol{r}}{r}$ to find

$$\Delta W_{\mathrm{el}} = \frac{1}{8\pi\varepsilon_0}\int_0^{R_{\mathrm{drop}}} (\varepsilon^{-1}(r) - 1)\frac{q^2}{r^2} dr. \tag{A21}$$

Assuming that the solvation energy is only determined by the electrostatic interactions, we set the Gibbs free energy $\Delta G_{\mathrm{solv}} = \Delta W_{\mathrm{el}}$ to obtain Eq. (13) of the main text. We finally note that, strictly speaking, our drop corresponds to an NVT ensemble and thus ΔW_{el} to the Helmholtz free energy for which, however, no experimental data are available. Yet, for the small solute inside the large water drop we expect Gibbs and Helmholtz free energies to be virtually identical.

[1] M. Chaplin, Do we underestimate the importance of water in cell biology?, Nat. Rev. Mol. Cell Biol. **7**, 861 (2006).

[2] P. Ball, Water: Water–an enduring mystery, Nature (London) **452**, 291 (2008).

[3] R. Baron, P. Setny, and J. Andrew McCammon, Water in cavity ligand recognition, J. Am. Chem. Soc. **132**, 12091 (2010).

[4] J. Li, J. M. Fernandez, and B. J. Berne, Water's role in the force-induced unfolding of ubiquitin, Proc. Natl. Acad. Sci. U.S.A. **107**, 19284 (2010).

[5] D. Thirumalai, G. Reddy, and J. E. Straub, Role of water in protein aggregation and amyloid polymorphism, Acc. Chem. Res. **45**, 83 (2012).

[6] S.-H. Chong and S. Ham, Interaction with the surrounding water plays a key role in determining the aggregation propensity of proteins, Angew. Chem. Int. Ed. **53**, 3961 (2014).

[7] Y. Levin, Polarizable Ions at Interfaces, Phys. Rev. Lett. **102**, 147803 (2009).

[8] D. Ben-Yaakov, D. Andelman, and R. Podgornik, Dielectric decrement as a source of ion-specific effects, J. Chem. Phys. **134**, 074705 (2011).

[9] W. Pezeshkian, N. Nikoofard, D. Norouzi, F. Mohammad-Rafiee, and H. Fazli, Distribution of counterions and interaction between two similarly charged dielectric slabs: Roles of charge discreteness and dielectric inhomogeneity, Phys. Rev. E **85**, 061925 (2012).

[10] M. Sega, S. S. Kantorovich, C. Holm, and A. Arnold, Communication: Kinetic and pairing contributions in the dielectric spectra of electrolyte solutions, J. Chem. Phys. **140**, 211101 (2014).

[11] I. Siretanu, D. Ebeling, M. P. Andersson, S. L. S. Stipp, A. Philipse, M. C. Stuart, D. van den Ende, and F. Mugele, Direct observation of ionic structure at solid-liquid interfaces: A deep look into the stern layer, Sci. Rep. **4**, 4956 (2014).

[12] M. Sega, S. Kantorovich, and A. Arnold, Kinetic dielectric decrement revisited: Phenomenology of finite ion concentrations, Phys. Chem. Chem. Phys. **17**, 130 (2015).

[13] N. Schwierz, D. Horinek, and R. R. Netz, Reversed anionic hofmeister series: The interplay of surface charge and surface polarity, Langmuir **26**, 7370 (2010).

[14] P. Lo Nostro and B. W. Ninham, Hofmeister phenomena: An update on ion specificity in biology, Chem. Rev. **112**, 2286 (2012).

[15] Y.-T. Kim, Y. Ito, K. Tadai, T. Mitani, U.-S. Kim, H.-S. Kim, and B.-W. Cho, Drastic change of electric double layer capacitance by surface functionalization of carbon nanotubes, Appl. Phys. Lett. **87**, 234106 (2005).

[16] S. Porada, B. B. Sales, H. V. M. Hamelers, and P. M. Biesheuvel, Water desalination with wires, J. Phys. Chem. Lett. **3**, 1613 (2012).

[17] J. R. Lakowicz, *Principles of Fluorescence Spectroscopy*, 3rd ed. (Springer, New York, 2006).

[18] The Bjerrum length denotes the distance at which the electrostatic interaction energy between two charged particles is equal to their thermal energy, the Debye length is a measure for the extent of electrostatic interactions in ionic solutions, and the Förster radius is the distance at which the energy transfer efficiency between a donor and an acceptor dye molecule equals 50%.

[19] W. Rocchia, E. Alexov, and B. Honig, Extending the applicability of the nonlinear poisson-boltzmann equation: Multiple dielectric constants and multivalent ions, J. Phys. Chem. B **105**, 6507 (2001).

[20] J. Dzubiella, J. M. J. Swanson, and J. A. McCammon, Coupling Hydrophobicity, Dispersion, and Electrostatics in Continuum Solvent Models, Phys. Rev. Lett. **96**, 087802 (2006).

[21] F. Fahrenberger, Z. Xu, and C. Holm, Simulation of electric double layers around charged colloids in aqueous solution of variable permittivity, J. Chem. Phys. **141**, 064902 (2014).

[22] D. Boda, D. Gillespie, W. Nonner, D. Henderson, and B. Eisenberg, Computing induced charges in inhomogeneous

dielectric media: Application in a monte carlo simulation of complex ionic systems, Phys. Rev. E **69**, 046702 (2004).
[23] M. Feliks, B. M. Martins, and G. M. Ullmann, Catalytic mechanism of the glycyl radical enzyme 4-hydroxyphenylacetate decarboxylase from continuum electrostatic and QC/MM calculations, J. Am. Chem. Soc. **135**, 14574 (2013).
[24] D. A. Egger, S. Weissman, S. Refaely-Abramson, S. Sharifzadeh, M. Dauth, R. Baer, S. Kümmel, J. B. Neaton, E. Zojer, and L. Kronik, Outer-valence electron spectra of prototypical aromatic heterocycles from an optimally tuned range-separated hybrid functional, J. Chem. Theory Comput. **10**, 1934 (2014).
[25] B. Klösgen, C. Reichle, S. Kohlsmann, and K. D. Kramer, Dielectric spectroscopy as a sensor of membrane headgroup mobility and hydration, Biophys. J. **71**, 3251 (1996).
[26] O. Teschke, G. Ceotto, and E. de Souza, Interfacial water dielectric-permittivity-profile measurements using atomic force microscopy, Phys. Rev. E **64**, 011605 (2001).
[27] U. Heugen, G. Schwaab, E. Brundermann, M. Heyden, X. Yu, D. M. Leitner, and M. Havenith, Solute-induced retardation of water dynamics probed directly by terahertz spectroscopy, Proc. Natl. Acad. Sci. U.S.A. **103**, 12301 (2006).
[28] R. Buchner and G. Hefter, Interactions and dynamics in electrolyte solutions by dielectric spectroscopy, Phys. Chem. Chem. Phys. **11**, 8984 (2009).
[29] K. Tielrooij, D. Paparo, L. Piatkowski, H. Bakker, and M. Bonn, Dielectric relaxation dynamics of water in model membranes probed by terahertz spectroscopy, Biophys. J. **97**, 2484 (2009).
[30] K.-J. Tielrooij, J. Hunger, R. Buchner, M. Bonn, and H. J. Bakker, Influence of concentration and temperature on the dynamics of water in the hydrophobic hydration shell of tetramethylurea, J. Am. Chem. Soc. **132**, 15671 (2010).
[31] B. Zhou, A. Kobayashi, H.-B. Cui, L.-S. Long, H. Fujimori, and H. Kobayashi, Anomalous dielectric behavior and thermal motion of water molecules confined in channels of porous coordination polymer crystals, J. Am. Chem. Soc. **133**, 5736 (2011).
[32] M. Hishida and K. Tanaka, Long-Range Hydration Effect of Lipid Membrane Studied by Terahertz Time-Domain Spectroscopy, Phys. Rev. Lett. **106**, 158102 (2011).
[33] U. Kaatze, Bound water: Evidence from and implications for the dielectric properties of aqueous solutions, J. Mol. Liq. **162**, 105 (2011).
[34] K. Mazur, R. Buchner, M. Bonn, and J. Hunger, Hydration of sodium alginate in aqueous solution, Macromolecules **47**, 771 (2014).
[35] H. A. Stern and S. E. Feller, Calculation of the dielectric permittivity profile for a nonuniform system: Application to a lipid bilayer simulation, J. Chem. Phys. **118**, 3401 (2003).
[36] S. Boresch, M. Willensdorfer, and O. Steinhauser, A molecular dynamics study of the dielectric properties of aqueous solutions of alanine and alanine dipeptide, J. Chem. Phys. **120**, 3333 (2004).
[37] V. Ballenegger and J.-P. Hansen, Dielectric permittivity profiles of confined polar fluids, J. Chem. Phys. **122**, 114711 (2005).
[38] M. C. F. Wander and A. E. Clark, Structural and dielectric properties of quartz-water interfaces, J. Phys. Chem. C **112**, 19986 (2008).
[39] M. Ahmad, W. Gu, T. Geyer, and V. Helms, Adhesive water networks facilitate binding of protein interfaces, Nat. Commun. **2**, 261 (2011).
[40] W. C. Guest, N. R. Cashman, and S. S. Plotkin, A theory for the anisotropic and inhomogeneous dielectric properties of proteins, Phys. Chem. Chem. Phys. **13**, 6286 (2011).
[41] D. J. Bonthuis, S. Gekle, and R. R. Netz, Dielectric Profile of Interfacial Water and its Effect on Double-Layer Capacitance, Phys. Rev. Lett. **107**, 166102 (2011).
[42] S. Gekle and R. R. Netz, Anisotropy in the dielectric spectrum of hydration water and its relation to water dynamics, J. Chem. Phys. **137**, 104704 (2012).
[43] A. Levy, D. Andelman, and H. Orland, Dielectric Constant of Ionic Solutions: A Field-Theory Approach, Phys. Rev. Lett. **108**, 227801 (2012).
[44] C. Zhang, F. Gygi, and G. Galli, Strongly anisotropic dielectric relaxation of water at the nanoscale, J. Phys. Chem. Lett. **4**, 2477 (2013).
[45] S. Parez, M. Předota, and M. Machesky, Dielectric properties of water at rutile and graphite surfaces: Effect of molecular structure, J. Phys. Chem. C **118**, 4818 (2014).
[46] K. F. Rinne, S. Gekle, and R. R. Netz, Dissecting ion-specific dielectric spectra of sodium-halide solutions into solvation water and ionic contributions, J. Chem. Phys. **141**, 214502 (2014).
[47] S. Gekle and R. R. Netz, Nanometer-resolved radio-frequency absorption and heating in biomembrane hydration layers, J. Phys. Chem. B **118**, 4963 (2014).
[48] A. A. Kornyshev and G. Sutmann, The shape of the nonlocal dielectric function of polar liquids and the implications for thermodynamic properties of electrolytes: A comparative study, J. Chem. Phys. **104**, 1524 (1996).
[49] M. V. Basilevsky and D. F. Parsons, An advanced continuum medium model for treating solvation effects: Nonlocal electrostatics with a cavity, J. Chem. Phys. **105**, 3734 (1996).
[50] F. O. Raineri, B.-C. Perng, and H. L. Friedman, A fluctuating charge density formulation of the dielectric behavior of liquids with applications to equilibrium and nonequilibrium solvation, Electrochim. Acta **42**, 2749 (1997).
[51] M. V. Basilevsky and D. F. Parsons, Nonlocal continuum solvation model with oscillating susceptibility kernels: A nonrigid cavity model, J. Chem. Phys. **108**, 9114 (1998).
[52] A. Hildebrandt, R. Blossey, S. Rjasanow, O. Kohlbacher, and H.-P. Lenhof, Novel Formulation of Nonlocal Electrostatics, Phys. Rev. Lett. **93**, 108104 (2004).
[53] M. V. Fedorov and A. A. Kornyshev, Unravelling the solvent response to neutral and charged solutes, Mol. Phys. **105**, 1 (2007).
[54] J. Rottler and B. Krayenhoff, Numerical studies of nonlocal electrostatic effects on the sub-nanoscale, J. Phys.: Condens. Matter **21**, 255901 (2009).
[55] B. Sahin and B. Ralf, Nonlocal and nonlinear electrostatics of a dipolar coulomb fluid, J. Phys.: Condens. Matter **26**, 285101 (2014).
[56] P. A. Bopp, A. A. Kornyshev, and G. Sutmann, Static Nonlocal Dielectric Function of Liquid Water, Phys. Rev. Lett. **76**, 1280 (1996).
[57] P. A. Bopp, A. A. Kornyshev, and G. Sutmann, Frequency and wave-vector dependent dielectric function of water: Collective modes and relaxation spectra, J. Chem. Phys. **109**, 1939 (1998).

[58] A. Kornyshev, Nonlocal screening of ions in a structurized polar liquid — new aspects of solvent description in electrolyte theory, Electrochim. Acta **26**, 1 (1981).

[59] See Supplemental Material at http://link.aps.org/supplemental/10.1103/PhysRevE.92.032718 for numerical checks.

[60] S. Pronk, S. Pall, R. Schulz, P. Larsson, P. Bjelkmar, R. Apostolov, M. R. Shirts, J. C. Smith, P. M. Kasson, D. van der Spoel, B. Hess, and E. Lindahl, GROMACS 4.5: A high-throughput and highly parallel open source molecular simulation toolkit, Bioinformatics **29**, 845 (2013).

[61] M. Fyta and R. R. Netz, Ionic force field optimization based on single-ion and ion-pair solvation properties: Going beyond standard mixing rules, J. Chem. Phys. **136**, 124103 (2012).

[62] W. Humphrey, A. Dalke, and K. Schulten, VMD – Visual Molecular Dynamics, J. Mol. Graphics **14**, 33 (1996).

[63] U. Essmann, L. Perera, M. L. Berkowitz, T. Darden, H. Lee, and L. G. Pedersen, A smooth particle mesh ewald method, J. Chem. Phys. **103**, 8577 (1995).

[64] D. J. Bonthuis, S. Gekle, and R. R. Netz, Profile of the static permittivity tensor of water at interfaces: Consequences for capacitance, hydration interaction and ion adsorption, Langmuir **28**, 7679 (2012).

[65] H. G. Petersen, Accuracy and efficiency of the particle mesh ewald method, J. Chem. Phys. **103**, 3668 (1995).

[66] M. Rami Reddy and M. Berkowitz, The dielectric constant of SPC/e water, Chem. Phys. Lett. **155**, 173 (1989).

[67] D. Chandler, Interfaces and the driving force of hydrophobic assembly, Nature (London) **437**, 640 (2005).

[68] K. J. Tielrooij, N. Garcia-Araez, M. Bonn, and H. J. Bakker, Cooperativity in ion hydration, Science **328**, 1006 (2010).

[69] M. Heyden, D. J. Tobias, and D. V. Matyushov, Terahertz absorption of dilute aqueous solutions, J. Chem. Phys. **137**, 235103 (2012).

[70] K. Shiraga, T. Suzuki, N. Kondo, and Y. Ogawa, Hydration and hydrogen bond network of water around hydrophobic surface investigated by terahertz spectroscopy, J. Chem. Phys. **141**, 235103 (2014).

[71] J. P. Bardhan, P. Jungwirth, and L. Makowski, Affine-response model of molecular solvation of ions: Accurate predictions of asymmetric charging free energies, J. Chem. Phys. **137**, 124101 (2012).

[72] A. Mukhopadhyay, A. T. Fenley, I. S. Tolokh, and A. V. Onufriev, Charge hydration asymmetry: The basic principle and how to use it to test and improve water models, J. Phys. Chem. B **116**, 9776 (2012).

[73] J. P. Bardhan and M. G. Knepley, Communication: Modeling charge-sign asymmetric solvation free energies with nonlinear boundary conditions, J. Chem. Phys. **141**, 131103 (2014).

[74] W. M. Latimer, K. S. Pitzer, and C. M. Slansky, The free energy of hydration of gaseous ions, and the absolute potential of the normal calomel electrode, J. Chem. Phys. **7**, 108 (1939).

[75] C. R. Corbeil, T. Sulea, and E. O. Purisima, Rapid prediction of solvation free energy. 2. the first-shell hydration (FiSH) continuum model, J. Chem. Theory Comput. **6**, 1622 (2010).

[76] A. V. Marenich, C. J. Cramer, and D. G. Truhlar, Universal solvation model based on the generalized born approximation with asymmetric descreening, J. Chem. Theory Comput. **5**, 2447 (2009).

[77] A. A. Rashin and B. Honig, Reevaluation of the born model of ion hydration, J. Phys. Chem. **89**, 5588 (1985).

[78] S. Rajamani, T. Ghosh, and S. Garde, Size dependent ion hydration, its asymmetry, and convergence to macroscopic behavior, J. Chem. Phys. **120**, 4457 (2004).

[79] $L^{(+)} = -274.9\,\mathrm{kJ/mol}/e^2$ and $L^{(-)} = -351.9\,\mathrm{kJ/mol}/e^2$ for ion parameters $\sigma_{iO} = 0.36051$ nm and $\epsilon_{iO} = 0.6388\,\mathrm{kJ/mol}$ [71].

[80] R. Schmid, A. M. Miah, and V. N. Sapunov, A new table of the thermodynamic quantities of ionic hydration: Values and some applications (enthalpy–entropy compensation and born radii), Phys. Chem. Chem. Phys. **2**, 97 (2000).

[81] W. R. Fawcett, Thermodynamic parameters for the solvation of monatomic ions in water, J. Phys. Chem. B **103**, 11181 (1999).